Supporting Information For

Band edge modulation via hydrogen-bond-free cation in hybrid bismuth iodine for overall photocatalytic CO$_2$ reduction

Guang-Ning Liu,[a,d,*] Cheng-Cheng Gao,[a] Fangzheng Qi,[a] Wen-Tong Chen,[c] Ning-Ning Zhang,[b] Yiqiang Sun,[a,*] Huaiqing Zhao,[a] Guozhu Chen[a] and Cuncheng Li[a,*]

[a]*School of Chemistry and Chemical Engineering, University of Jinan, Jinan, Shandong 250022, P. R. China*

[b]*College of Chemistry and Chemical Engineering, Liaocheng University, Liaocheng, 252059, P. R. China*

[c]*Institute of Applied Chemistry, School of Chemistry and Chemical Engineering, Jinggangshan University, Ji'an, Jiangxi 343009, China*

[d]*State Key Laboratory of Structural Chemistry, Fujian Institute of Research on the Structure of Matter, Chinese Academy of Sciences, Fuzhou, Fujian 350002, P. R. China*

E-mail: chm_liugn@ujn.edu.cn (G.-N. Liu), chm_licc@ujn.edu.cn (C. C. Li).

S1 Experimental Section

S1.1 Materials and characterization

All reagents were purchased commercially and used without further purification. Elemental analyses of C, H, and N were performed on an Elementar Vario EL III microanalyzer. Powder X-ray diffraction (PXRD) patterns were recorded on Bruker D8 Focus diffractometer using Cu $K\alpha$ radiation. CrystalExplorer21 software was used to quantitatively analyze the intermolecular interaction in the crystal structures. A Perkin-Elmer Diamond thermogravimetric analyzer was used to obtain thermogravimetric analyses (TGA) curves in N_2 with a flow rate of 20 mL·min^{-1} and a ramp rate of 10 °C·min^{-1} in the temperature range 30–800 °C. An empty Al_2O_3 crucible was used as the reference. The FT-IR spectra were obtained in the range 400-4000 cm^{-1} on a PerkinElmer FT-IR spectrometer using KBr pellets. Optical diffuse reflectance spectra were measured at room temperature with a Shimadzu UV-3101 PC UV-vis spectrophotometer. The instrument was equipped with an integrating sphere and controlled with a personal computer. The samples were ground into fine powder and pressed onto a thin glass slide holder. A $BaSO_4$ plate was used as a standard (100% reflectance). The absorption spectra were calculated from reflectance spectrum using the Kubelka-Munk function: $\alpha/S = (1-R)^2/2R$ where α is the absorption coefficient, S is the scattering coefficient (which is practically wavelength independent when the particle size is larger than 5 μm), and R is the reflectance. The photocatalytic experimental instrument is Labsolar 6A equipment of PerfectLight, and the gas chromatography instrument is GC2010PLUS model of Shimadzu. The CO_2 adsorption tests were measured using a CO_2 adsorption instrument (Micromeritics ASAP2420, America).

S1.2 Computational details

The X-ray crystallographic data of **1**–**2** were used to calculate its electronic structure. The calculations of density of states (DOS) were carried out using density functional theory (DFT) with one of the three nonlocal gradient-corrected exchange-correlation functionals (GGA-PBE) and performed with the CASTEP code, which uses a plane wave basis set for the valence electrons and norm-conserving pseudopotential for the core electrons.[1] The number of

plane waves included in the basis was determined by a cutoff energy, E_c, of 280 eV for **1** and **2**. Pseudo-atomic calculations were performed for Bi $5d^{10}6s^26p^3$, I $5s^25p^6$, C $2s^22p^2$, N $2s^22p^3$, O $2s^22p^4$ and H $1s^1$. The parameters used in the calculations and convergence criteria were set by the default values of the CASTEP code.

S1.3 Single-crystal structure determination

The intensity data sets of **1** and **2** were collected on a Agilent Xcalibur, Eos, Gemini CCD diffractometer equipped with a graphite-monochromated Mo Kα radiation (λ = 0.71073 Å) at 293 K. The data sets were reduced by the CrysAlisPro program.[2] An empirical absorption correction using spherical harmonics was implemented in SCALE3 ABSPACK scaling algorithm. The structures were solved by direct methods using the Siemens SHELXL package of crystallographic software. Difference Fourier maps were created on the basis of these atomic positions to yield the other non-hydrogen atoms. The structures were refined using a full-matrix least-squares refinement on F2. All non-hydrogen atoms were refined anisotropically. The hydrogen atoms of **1** and **2** were located at geometrically calculated positions and refined as riding on their parent atoms with fixed isotropic displacement parameters [Uiso(H) = 1.2Ueq(C, N)]. Crystallographic data and structural refinements for **1** and **2** are summarized in Table S1. Important bond lengths and angles are listed in Table S2.

S1.4 Photoelectrochemical Property Study

Photocurrent and electrochemical impedance spectroscopy (EIS) were carried out in a conventional three-electrode system on the Solartron ModuLab XM platform by using 0.1 M KCl electrolyte, and the irradiation area was 1 cm^2 under a 500 W Xe lamp (CEL-S500, Beijing China Education Au-light Co., Ltd). The working electrodes were prepared as follows: 10 mg of the as-prepared and finely ground powders of **1** and **2** were dispersed in 10 mL ethanol to produce a suspension, which was then coated onto a 1 × 1 cm^2 FTO glass electrode and dried at 40 °C under a vacuum condition for 2 h. A Pt foil as the counter electrode and an Ag/AgCl electrode as a reference electrode were used. The photocurrent was measured at 2 V. The EIS was performed at a bias voltage of 0.5 mV and a frequency range of $10-10^5$ Hz.

S1.5 In situ DRIFTS measurement

In situ diffuse reflectance infrared Fourier-transform spectroscopy (DRIFTS) experiments were conducted on a Bruker (TensorII) FT-IR spectrometer. The powders of **2** were carefully flattened on a sample holder to enhance the IR reflection. The sample was washed with a N_2 stream at 120 °C to eliminate physisorbed gaseous impurities. After the pretreatment, moist CO_2 with water vapor was introduced into the reactor until saturation adsorption. A simulated sunlight was used to drive the in situ photocatalytic reaction.

S1.6 Syntheses of 1 and 2

Preparation of 1. A mixture of BiI_3 (0.236 g, 0.4 mmol), Hbiz (0.054 g, 0.46 mmol), concentrated HI (0.3 mL, 45%) and 5.0 mL acetone were sealed in a 25-mL poly(tetrafluoroethylene)-lined stainless steel container under autogenous pressure and then heated at 120 °C for 3 days and finally cooled to room temperature. Red block crystals were obtained and washed with ethanol (Yield: 90% based on Bi). Elemental analysis calcd. (%) for **1** $C_7H_9N_2OBiI_4$: C 9.85, N 3.28, H 1.06; found: C 10.20, N 3.32, H 1.01.

Preparation of 2. A mixture of BiI_3 (0.236 g, 0.4 mmol), Hbiz (0.054 g, 0.46 mmol), concentrated HI (0.3 mL, 45%), 5.0 mL acetone and 1.0 mL methyl alcohol were sealed in a 25-mL poly(tetrafluoroethylene)-lined stainless steel container under autogenous pressure and then heated at 120 °C for 3 days and finally cooled to room temperature. Red needle crystals were obtained and washed with ethanol (Yield: 97% based on Bi). Elemental analysis calcd. (%) for **2** $C_9H_{11}N_2BiI_4$: C 12.51, N 3.24, H 1.28; found: C 12.69, N 3.33, H 1.27.

S2. Results and discussion

Table S1. Crystal and Structure Refinement Data for **1** and **2**.

Compound	1	2
CCDC Number	2336516	2336517
Empirical formula	$C_9H_{11}N_2BiI_4$	$C_7H_8N_2OBiI_4$
Formula weight	863.78	852.73
Crystal system	triclinic	triclinic
Space group	P-1	P-1
a/Å	7.6058(4)	7.6459(3)
b/Å	10.8679(5)	9.8910(4)
c/Å	11.5758(5)	11.4115(5)
α/°	79.148(4)	74.820(4)
β/°	77.920(4)	86.247(3)
γ/°	72.081(4)	83.582(3)
Volume/Å^3	882.34(8)	827.08(6)
Z	2	2
ρ_{calc} g/cm^3	3.251	3.424
μ/mm^{-1}	16.971	18.106
F(000)	748.0	734.0
2θ range /°	5.974 to 51	6.344 to 51
Reflections collected	10152	9503
Independent reflections (R_{int})	3280(0.0374)	3075 (0.0303)
Data/restraints/parameters	3280/0/148	3075/0/140
GOF on F^2	1.022	1.049
R_1[a], wR_2[b] [I>=2σ (I)]	0.0299, 0.0601	0.0253, 0.0532
Largest diff. peak/hole / e Å^{-3}	0.97/ -0.98	1.11/-0.91

[a] $R_1 = \sum||F_o|-|F_c||/\sum|F_o|$, [b] $wR_2 = \{\sum w[(F_o)^2-(F_c)^2]^2/\sum w[(F_o)^2]^2\}^{1/2}$

Table S2. Selected Bond Distances (Å) and Angles (°) for **1** and **2**.

1			
Bond	(Å)	Bond	(Å)
Bi(1)-I(1)	3.085(5)	N(2)-C(7)	1.322(12)
Bi(1)-I(2)	2.902(5)	C(1)-C(2)	1.357(12)
Bi(1)-I(3)	2.921(5)	C(1)-C(6)	1.381(9)
Bi(1)-I(4)	3.090(5)	C(2)-C(3)	1.324(14)
Bi(1)-I(4)#1	3.272(5)	C(3)-C(4)	1.413(14)
N(1)-C(1)	1.379(11)	C(4)-C(5)	1.324(11)
N(1)-C(7)	1.275(13)	C(5)-C(6)	1.363(10)
N(2)-C(6)	1.388(10)		
Angle	(°)	Angle	(°)
I(2)-Bi(1)-I(1)	89.493(14)	C(2)-C(1)-N(1)	134.6(8)
I(3)-Bi(1)-I(1)	95.151(15)	C(6)-C(1)-N(1)	105.0(8)
I(3)-Bi(1)-I(2)	95.022(17)	C(6)-C(1)-C(2)	120.4(9)
I(4)-Bi(1)-I(1)	171.845(15)	C(3)-C(2)-C(1)	118.4(9)
I(4)#1-Bi(1)-I(1)	89.058(13)	C(4)-C(3)-C(2)	120.7(10)
I(4)-Bi(1)-I(2)	96.219(15)	C(5)-C(4)-C(3)	121.6(10)
I(4)#1-Bi(1)-I(2)	88.519(15)	C(6)-C(5)-C(4)	117.2(8)
I(4)-Bi(1)-I(3)	90.156(15)	C(1)-C(6)-N(2)	106.8(7)
I(4) #1-Bi(1)-I(3)	174.515(14)	C(5)-C(6)-N(2)	131.5(7)
C(7)-N(1)-C(1)	110.2(9)	C(5)-C(6)-C(1)	121.7(8)
C(7)-N(2)-C(6)	107.1(8)	N(2)-C(7)-N(1)	110.9(10)

Symmetry transformations used to generate equivalent atoms: #1 -*x*, 2-*y*, 1-*z*.

	2		
Bond	(Å)	Bond	(Å)
Bi(1)-I(1) #1	3.288(6)	N(1)-C(9)	1.458(10)
Bi(1)-I(1)	3.099(5)	N(2)-C(6)	1.384(9)
Bi(1)-I(2)	3.073(6)	N(2)-C(8)	1.311(9)
Bi(1)-I(2) #2	3.286(6)	N(2)-C(7)	1.465(9)
Bi(1)-I(3)	2.919(6)	C(6)-C(1)	1.388(10)
Bi(1)-I(4)	2.927(6)	C(6)-C(5)	1.394(10)
I(1)-Bi(1)#1	3.288(6)	C(1)-C(2)	1.388(10)
I(2)-Bi(1)#2	3.286(6)	C(5)-C(4)	1.364(12)
N(1)-C(1)	1.380(8)	C(2)-C(3)	1.377(12)
N(1)-C(8)	1.321(9)	C(4)-C(3)	1.409(14)

Angle	(°)	Angle	(°)
I(1)-Bi(1)-I(1)#1	86.670(15)	C(1)-N(1)-C(9)	126.4(7)
I(1)-Bi(1)-I(2)#2	87.820(15)	C(8)-N(1)-C(1)	107.3(6)
I(2)-Bi(1)-I(1)	172.654(16)	C(8)-N(1)-C(9)	126.2(7)
I(2)#2-Bi(1)-I(1)#1	84.250(15)	C(6)-N(2)-C(7)	126.5(6)
I(2)-Bi(1)-I(1)#1	87.421(15)	C(8)-N(2)-C(6)	107.6(6)
I(2)-Bi(1)-I(2)#2	87.250(14)	C(8)-N(2)-C(7)	125.9(7)
I(3)-Bi(1)-I(1)	88.951(16)	N(2)-C(6)-C(1)	106.5(6)
I(3)-Bi(1)-I(1)#1	172.355(16)	N(2)-C(6)-C(5)	131.3(8)
I(3)-Bi(1)-I(2)#2	89.327(17)	C(1)-C(6)-C(5)	122.3(8)
I(3)-Bi(1)-I(2)	96.431(17)	N(1)-C(6)-C(5)	106.8(7)
I(3)-Bi(1)-I(4)	93.406(17)	N(1)-C(1)-C(2)	131.3(8)
I(4)-Bi(1)-I(1)#1	93.291(16)	C(6)-C(1)-C(2)	121.9(7)
I(4)-Bi(1)-I(1)	96.141(17)	C(4)-C(5)-C(6)	115.6(9)
I(4)-Bi(1)-I(2)#2	175.222(16)	N(2)-C(8)-N(1)	111.8(7)
I(4)-Bi(1)-I(2)	88.549(16)	C(3)-C(2)-C(1)	116.0(9)
Bi(1)-I(1)-Bi(1)#1	93.330(14)	C(5)-C(4)-C(3)	122.5(9)
Bi(1)-I(2)-Bi(1)#2	92.750(15)	C(2)-C(3)-C(4)	121.7(9)

Symmetry transformations used to generate equivalent atoms: #1 2-*x*, -*y*, -*z*; #2 1-*x*, -*y*, -*z*.
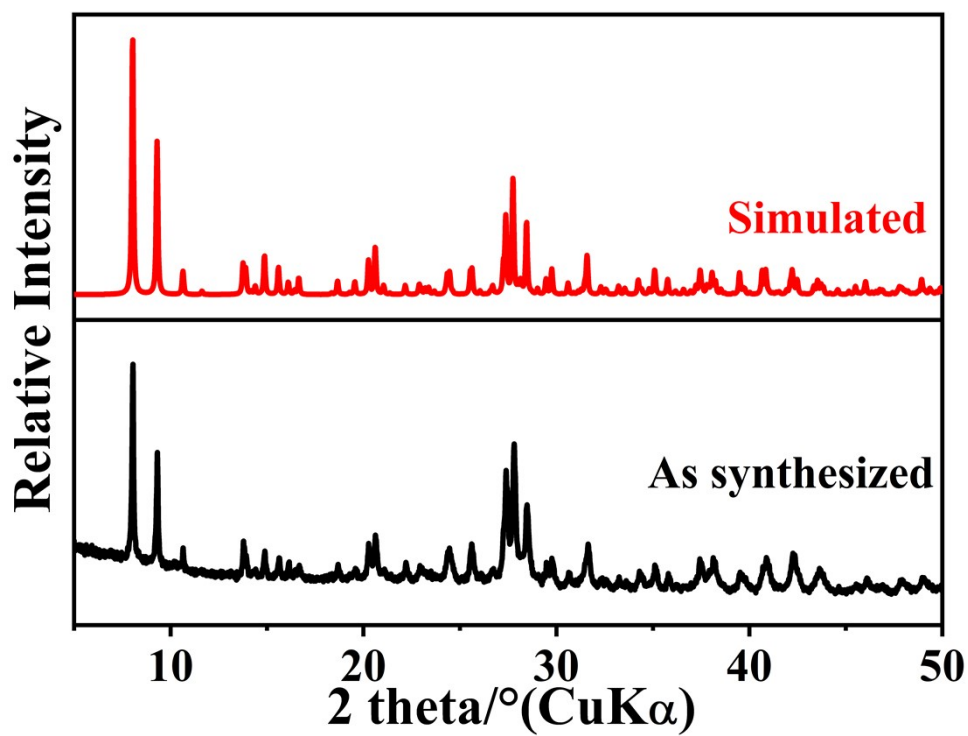
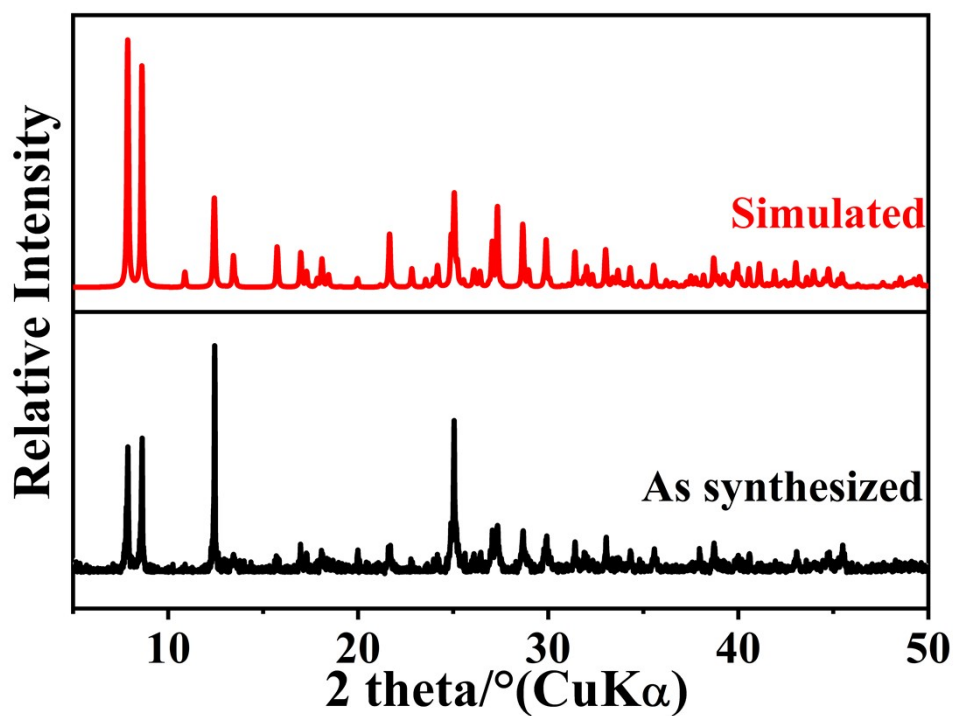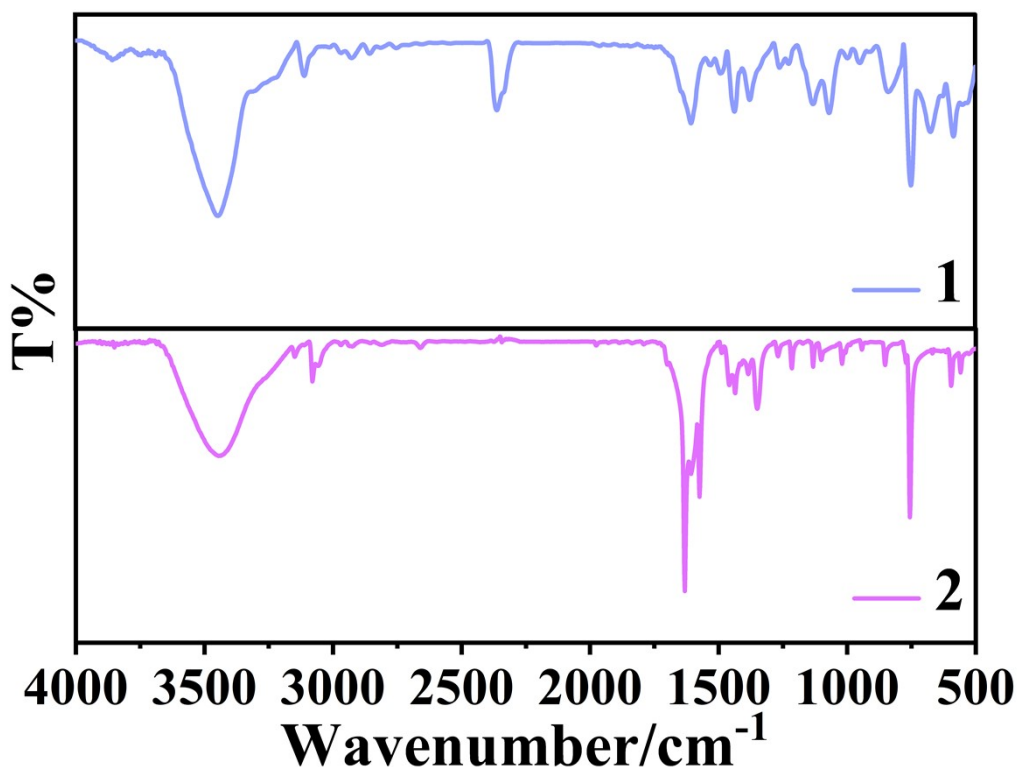**Figure S1.** The simulated and experimental PXRD patterns for **1**.

Figure S2. The simulated and experimental PXRD patterns for **2**.

Figure S3. IR spectra of **1** and **2**.

IR analyses: Both compounds show a strong peak near 3450 cm^{-1}, which is caused by water molecules in the air.[3] The 3100-3000 cm^{-1} region corresponds to the C-H stretching vibration on the benzene ring. In addition, the characteristic benzene ring vibration (ν(C=C) and ν(C=N)) was observed at 1600-1400 cm^{-1} for both compounds, confirming the successful introduction of biz-derivative cations. Further, the existence of the protonated and alkylated imidazole-N products in **1** and **2** can also be confirmed by their IR spectra. The IR bands at 2950–2845 cm^{-1} are attributed to the N–H$^+$ stretching vibrations of $\equiv$NH$^+$ for **1**. The occurrence of the characteristic band of –CH$_3$ around 1380 cm^{-1} confirms the presence of methylated biz cation in **2**. All the analyses are in agreement with the results of single crystal X-ray diffraction studies.

Table S3. Polyhedron Distortions of the (BiI_4) Units in **1** and **2**.

Compound	Units	Max(Bi-I valence)	Min(Bi-I valence)	ΔR
1	(BiI_6)	2.340	2.026	7.415×10^{-4}
2	(BiI_6)	2.307	2.267	9.616×10^{-3}

The Δ*R* is proposed by Brown to evaluate the distortion of a polyhedron, where a larger value means a more serious distorted geometry.[4] Generally, a larger ΔR value means a more serious distorted polyhedron geometry. The ΔR can be calculated by the equation.[5]

$$\Delta R = -(0.37/N)\sum \ln(S_i/S')$$

where N is the number of bonds formed by the Bi atom, S_i is the valence of the Bi–I bond and S' is the average valence of the Bi–I bonds in the (BiI_6) coordination sphere.

Table S4. Selected Hydrogen Bonds Data for **1**.

D-H···A	D-H (Å)	H···A (Å)	D···A (Å)	∠DHA (°)
N1-H1···I1	0.860	2.845	3.688	167.20
N2-H2···O1	0.860	1.885	2.736	169.70
O1-H1A···I4[a]	0.850	2.817	3.555	146.11
O1-H1B···O1[b]	0.849	2.436	2.912	116.15

Symmetry codes: a (-*x*, -*y*+1, -*z*+1), b (-*x*, -*y*, -*z*+2).
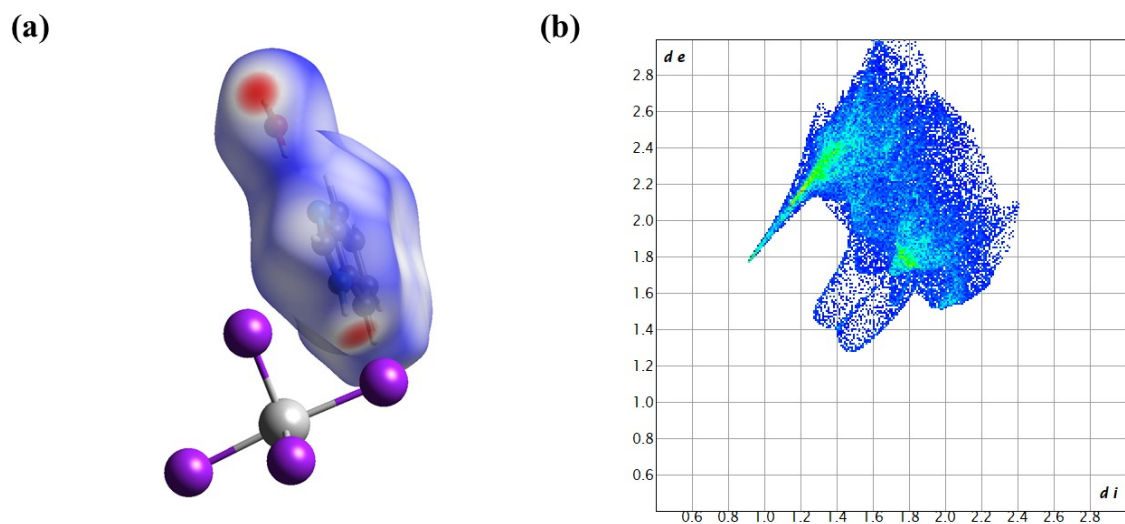
Figure S4. (a) Hirshfeld surface mapped over d_{norm} for $(H_2biz)^+$ in **1**. (b) Two dimensional fingerprint plot of **1**.
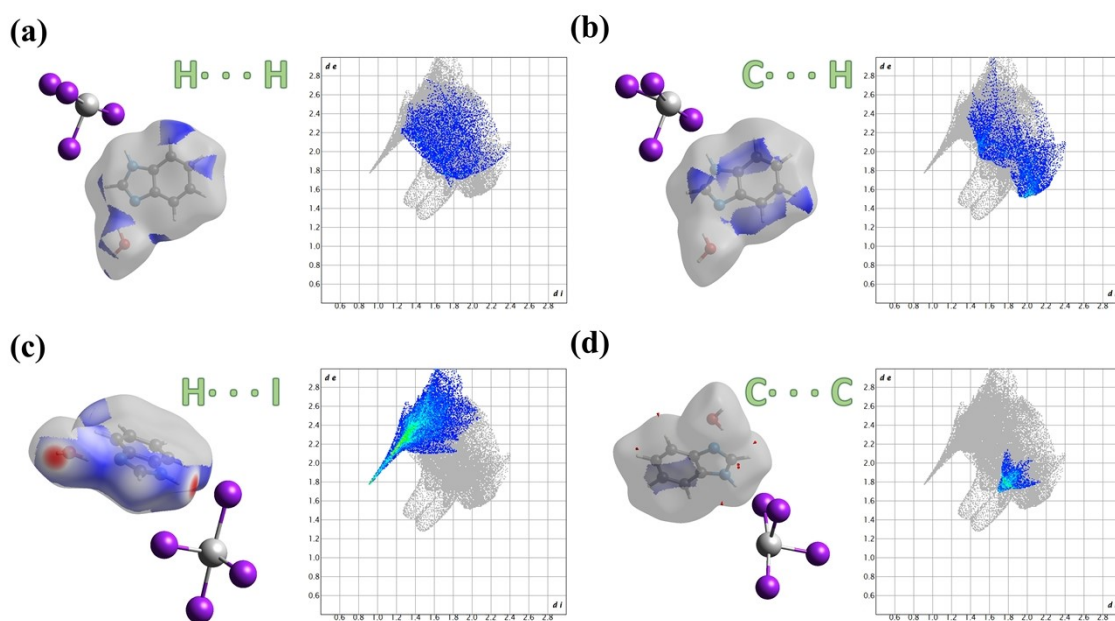
**Figure S5.** The 2D fingerprint plots with a d_{norm} view of the (a) H···H (12.7%), (b) C···H/H···C (16.1%), (c) H···I/I···H (41.3%) and (d) C···C (7.6%) in **1**.
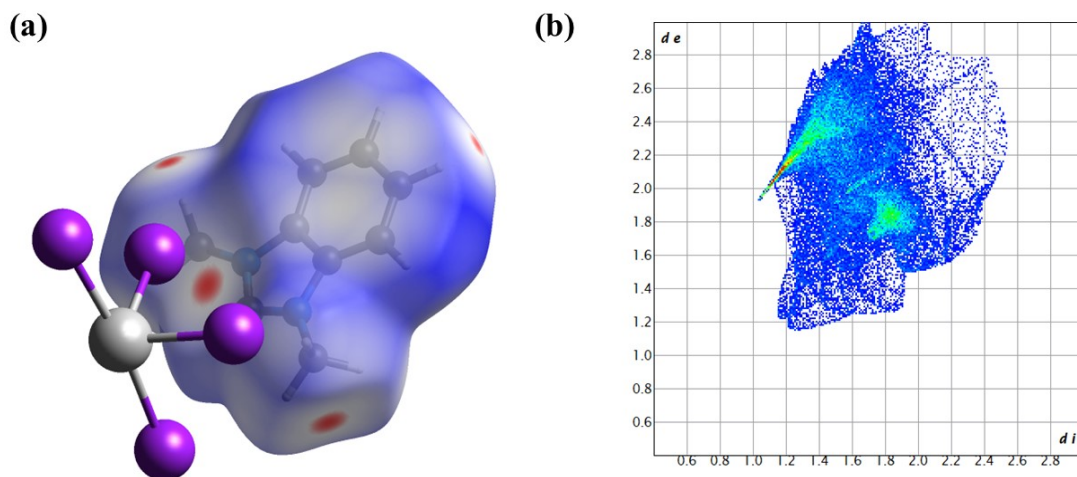
Figure S6. (a) Hirshfeld surface mapped over d_{norm} for (Me$_2$biz)$^+$ in **2**. (b) Two dimensional fingerprint plot of **2**.
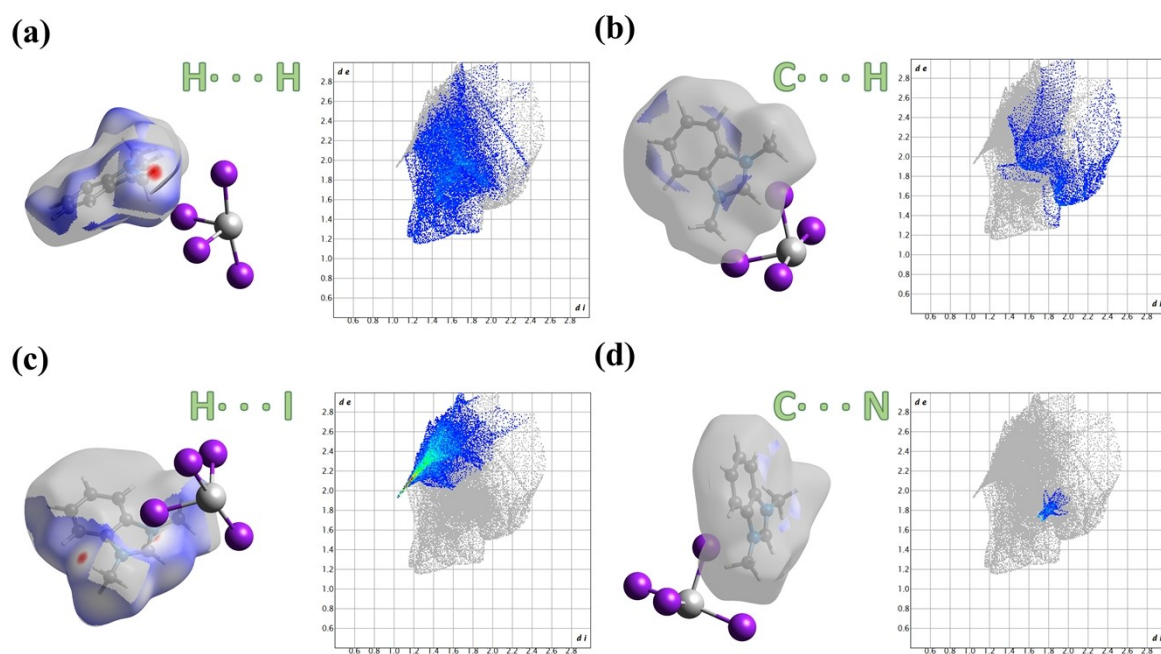
Figure S7. The 2D fingerprint plots with a d_{norm} view of the (a) H···H (37.4%), (b) C···H/H···C (12.7%), (c) H···I/I···H (36.4%) and (d) C···N/N···C (2.0%) in **2**.

Noncovalent interaction analyses:

The different colors in the Hirshfeld surfaces indicate different contacts between neighboring atoms. The red color indicates the contact distance shorter than sum of van der Waals (vdW) radii, which indicates the presence of typical non-covalent interactions e.g., hydrogen bonds. The white color indicates the distance approaches the sum of vdW radii. Blue color suggests the distance is longer than vdW separation, too far to interact with neighboring atom.[6] The H···I/I···H interactions accounts for 41.3% of the total Hirschfeld surface interactions in **1**. More detailed structural analysis shows that the nearest centroid to centroid distance between adjacent benzene rings is much greater than 3.8 Å. This result suggests that there are centroid to centroid π···π interactions in **1** and **2**.
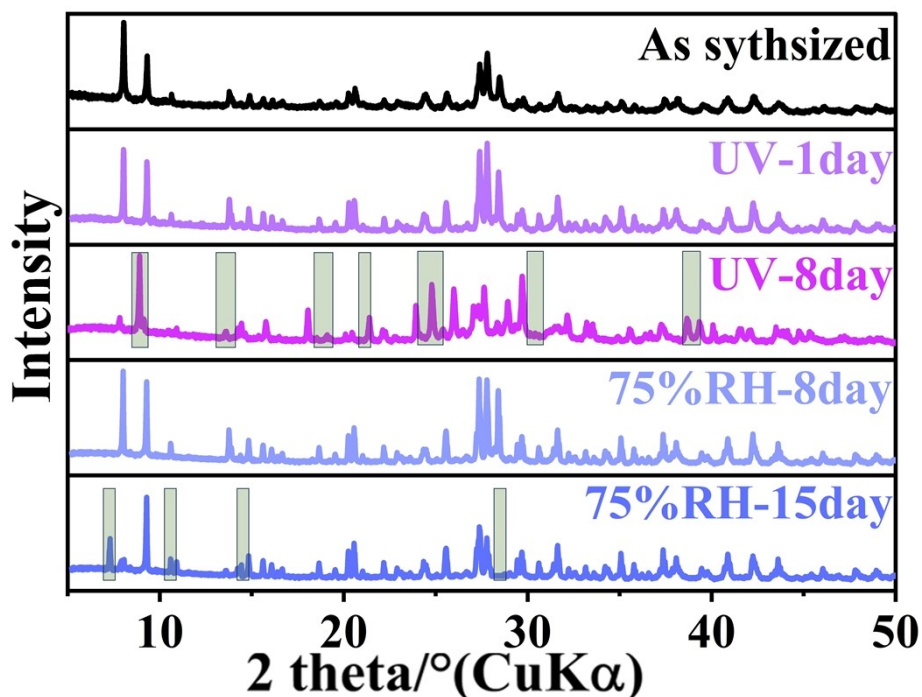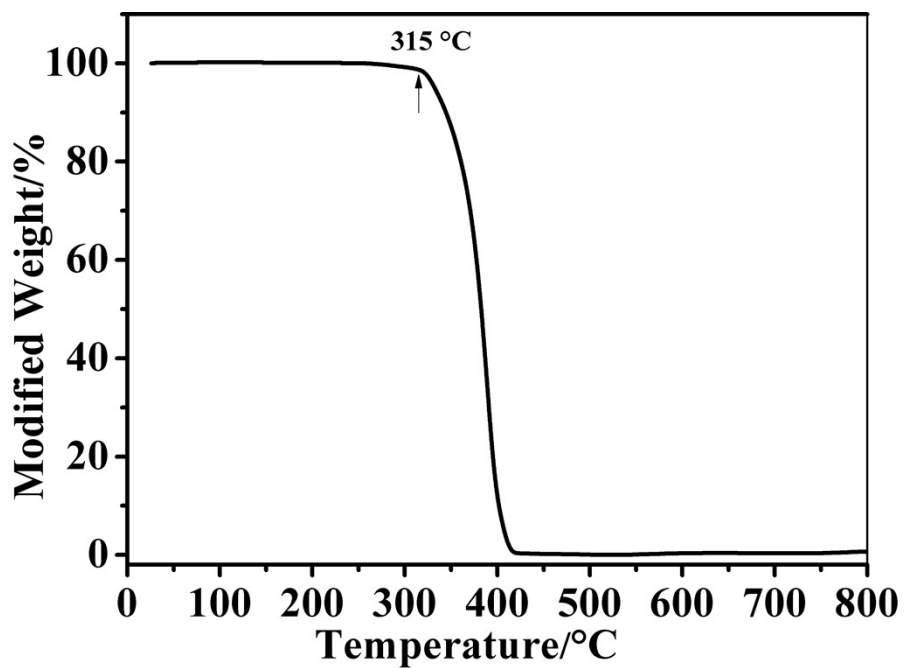
Figure S8. PXRD patterns of **1** under different conditions. The unmatched diffraction peaks were marked.
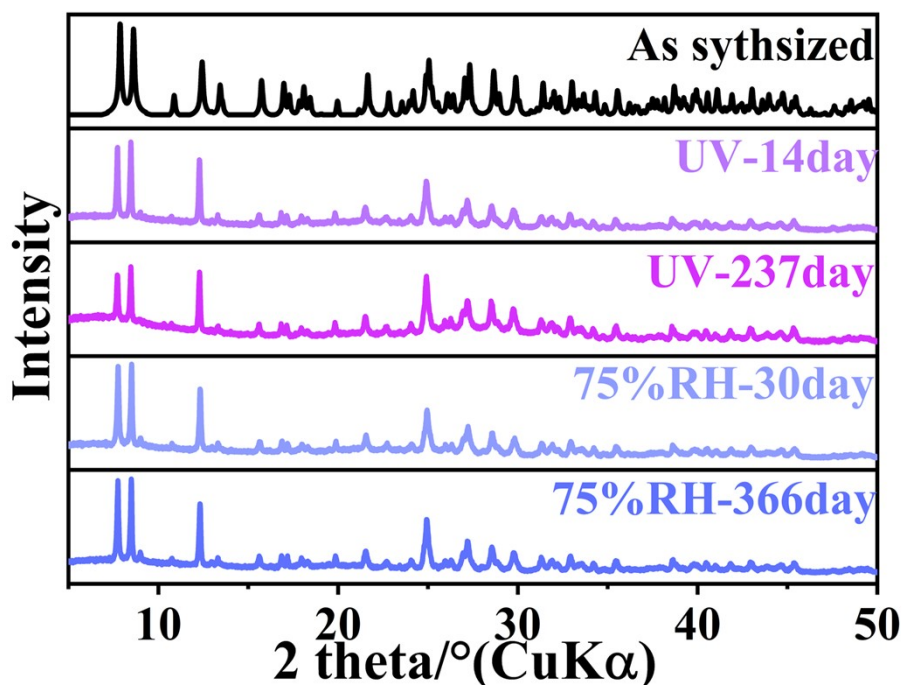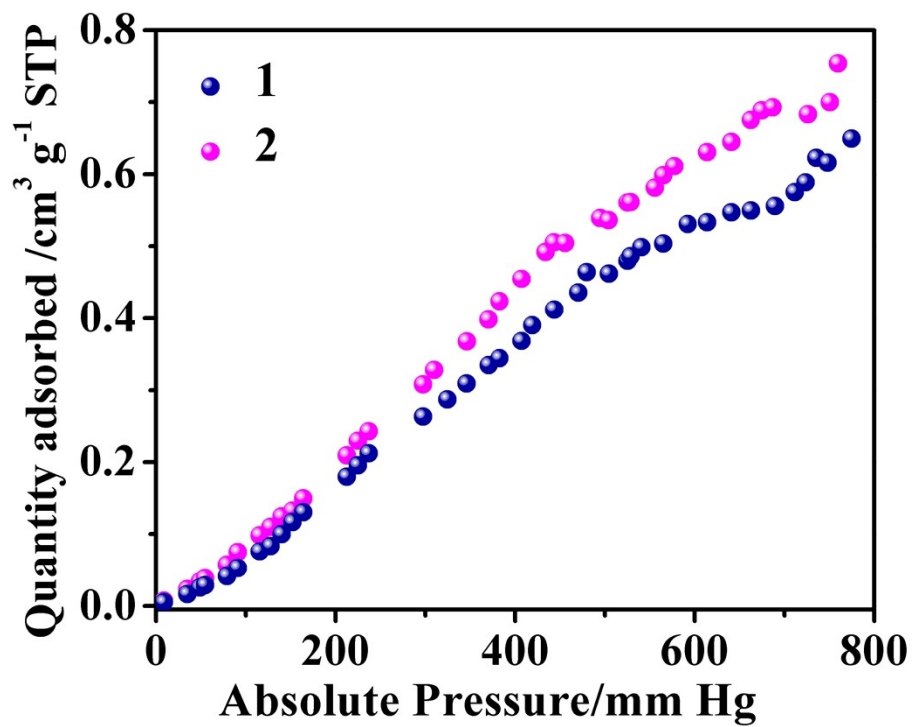

Figure S9. PXRD patterns of **2** under different conditions.
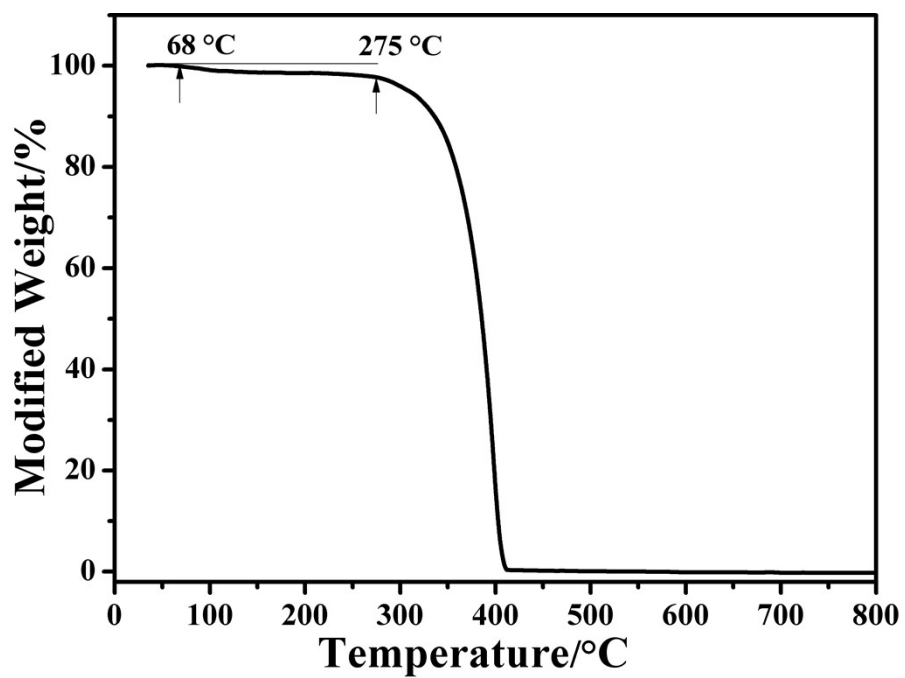
Figure S10. TGA curve for **1**. The temperatures at which the lattice water molecules release and the the framework collapses were labeled.

Figure S11. TGA curve for **2**. The temperature at which the framework collapses was marked.
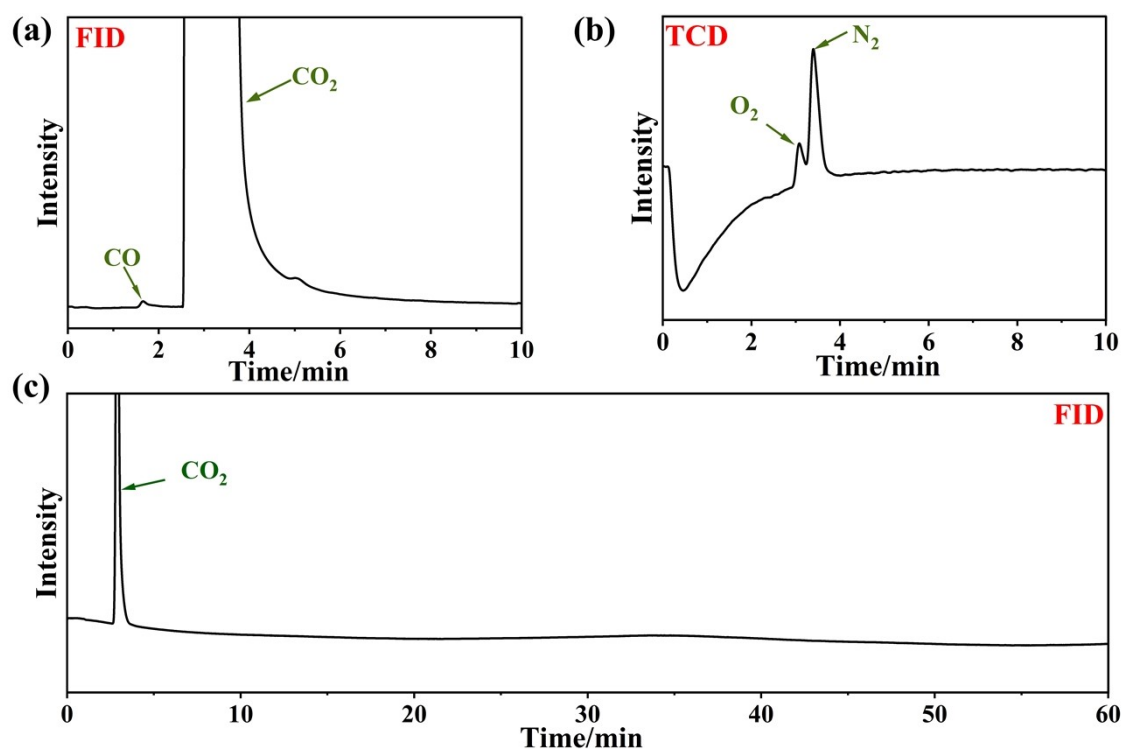
Figure S12. CO_2 absorption isotherms of **1** and **2** at 298 K.

Figure S13. Full view of the photocatalytic reaction equipment.

Figure S14. The detection of the PCR products with **2** as the photocatalyst. (a) The gas chromatogram of FID detector. (b) The gas chromatogram of TCD detector. (c) The chromatogram obtained by detecting the liquid product with FID detector.

Table S5. Summary of the PCR Details with Bi-based Perovskites and Selected Hybrid Perovskites as Photocatalysts.

Photocatalyst	Reaction medium (Reaction system)	Products and Yield ($\mu mol \cdot g^{-1} \cdot h^{-1}$)	Refs
$MA_3Bi_2I_9$/OA, OLA	CO_2/H_2O vapor (solid–gas)	CO: 0.72 CH_4: 0.98	[7]
$Cu_6(HL_1)_2(L_1)_4(PF_6)_2$	CO_2/H_2O vapor (solid–gas)	CO: 24.8	[8]
$Au_{0.19}/[Pb_8I_8(H_2O)_3]^{8+}[^-O_2C(CH_2)_4CO^{2-}]_4$	H_2O (solid–liquid)	CO: 84.2	[9]
$FAPbBr_3$	Ethyl acetate/H_2O (solid–liquid)	CO: 181.25 CH_4: 16.9	[10]
$FAPbBr_3/PbI_2$	CO_2/H_2O vapor (solid–gas)	CO: 10.29 CH_4: 1.09	[11]
$FAPbBr_3/Ti_3C_2$	H_2O (solid–liquid)	CO: 182.87 CH_4: 11.59	[12]
$FAPbBr_3$/a-Fe_2O_3	CO_2/H_2O vapor (solid–gas)	CO: 45.5 CH_4: 10.5	[13]
$MAPbBr_3$/Ni(ppy)/SiO_2	H_2O or EA/H_2O (solid–liquid)	CO: 2.66	[14]
$MAPbI_3$@PCN-221($Fe_{0.2}$)	Ethyl acetate/H_2O (solid–liquid)	CO: 4.16 CH_4: 13.00	[15]
$(ha)_2CsPb_2Br_7$	Butyl acetate (solid–liquid)	CO: 158.69 CH_4: 6.9	[16]
$Rb_3Bi_2I_9$	CO_2/H_2O vapor (solid–gas)	CO: 18.2 CH_4: 17.0	[7]
$Cs_3Bi_2I_9$	CO_2/H_2O vapor (solid–gas)	CO: 7.76 CH_4: 1.49	[7]
$Cs_3Bi_2Br_9$	CO_2/H_2O vapor (solid–gas)	CO: 26.95	[17]
$Cs_3Bi_2(Br_{0.5}I_{0.5})_9$	CO_2/H_2O vapor (solid–gas)	CO: 18	[18]
$Cs_3Bi_2(Cl_{0.5}Br_{0.5})_9$	CO_2/H_2O vapor (solid–gas)	CO: 16	[18]
$Cs_3Bi_2I_9/Bi_2WO_6$	H_2O (solid–liquid)	CO: 7.33	[19]
MCM-41@$Cs_3Bi_2Br_9$	H_2O (solid–liquid)	CO: 17.24	[20]

$In_4SnS_8/Cs_3Bi_2Br_9$	H_2O (solid–liquid)	CO: 9.55	[21]
$Au-Cs_3Bi_2Br_9/V_2O_5$	CO_2/H_2O (solid–gas)	CO: 98.95	[22]
$Cs_3Bi_2Br_9/\alpha-Fe_2O_3$	CO_2/H_2O (solid–gas)	CO: 84.12	[23]
$Cs_2AgBiBr_6$	Ethyl acetate (solid–liquid)	CO: 2.35 CH$_4$: 1.60	[24]
$Cs_2AgBiBr_6/Ti_3C_2Tx$	H_2O (solid–liquid)	CO: 11.1 CH$_4$: 1.3	[25]
$Cs_2AgBiBr_6/Ce-UiO-66-H$	H_2O (solid–liquid)	CO: 309.01	[26]
$Cs_2AgBiBr_6/Bi_2WO_6$	EA/IPA (solid–liquid)	CO: 42.19 CH$_4$: 0.41	[27]
$Cs_2AgBiBr_6/Sr_2FeNbO_6$	Ethyl acetate/H_2O (solid–liquid)	CO: 50 CH$_4$: 8.12	[28]
$TiO_2/Cs_2AgBiBr_6$	Ethyl acetate (solid–liquid)	CO: 5.72 CH$_4$: 8.46	[29]
$Cs_2AgBiBr_6-Cu-rGO$	CO_2/H_2O (solid–gas)	CO: 1.9 CH$_4$: 10.7	[30]
$(Me_2biz)BiI_4$	H_2O (solid–liquid)	CO: 2.19	This work

Abbreviations: MA: $CH_3NH_3^+$; OA: oleic acid; OLA: oleylamine; FA: formamidinium; ha: hexylammonium; rGO: reduced graphene oxide.
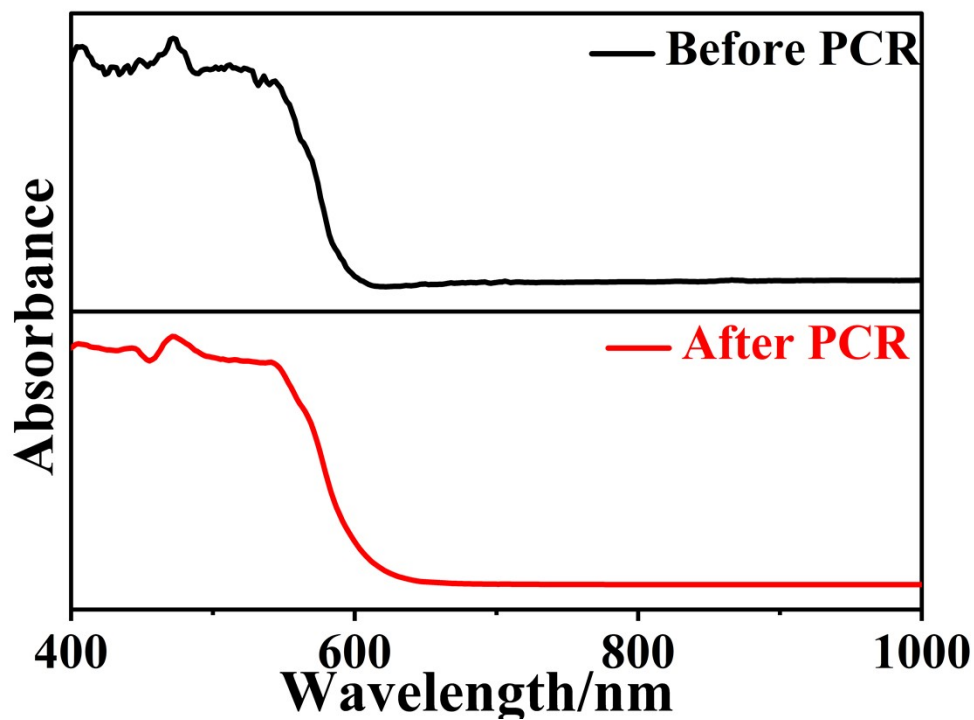
Figure S15. Solid state absorption plots of **2** before and after PCR reactions.
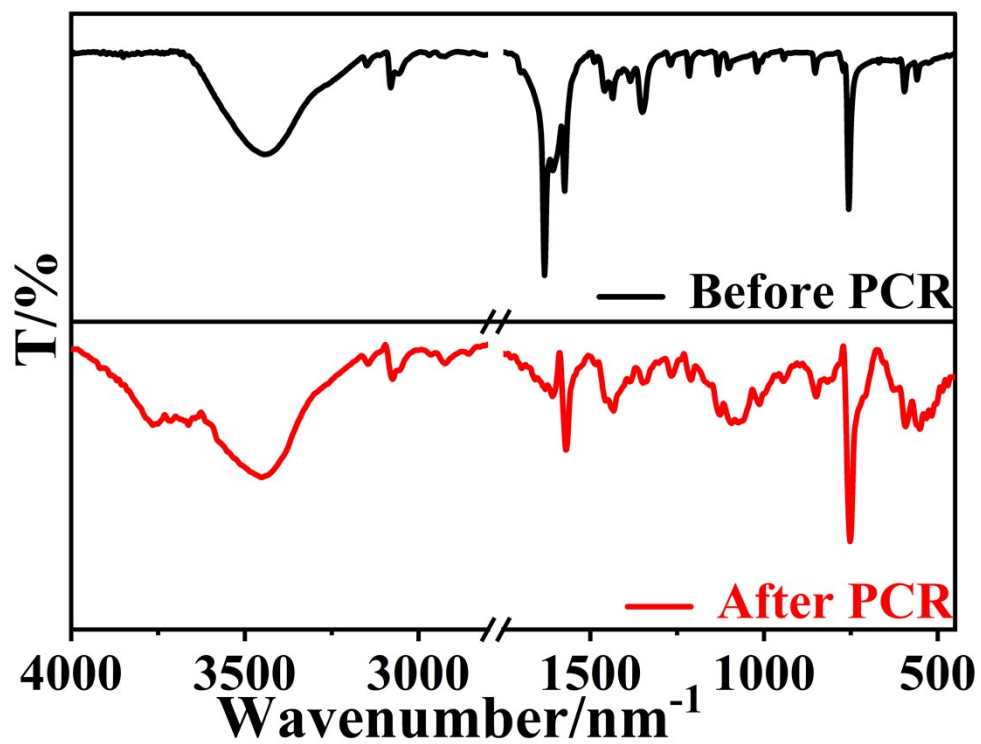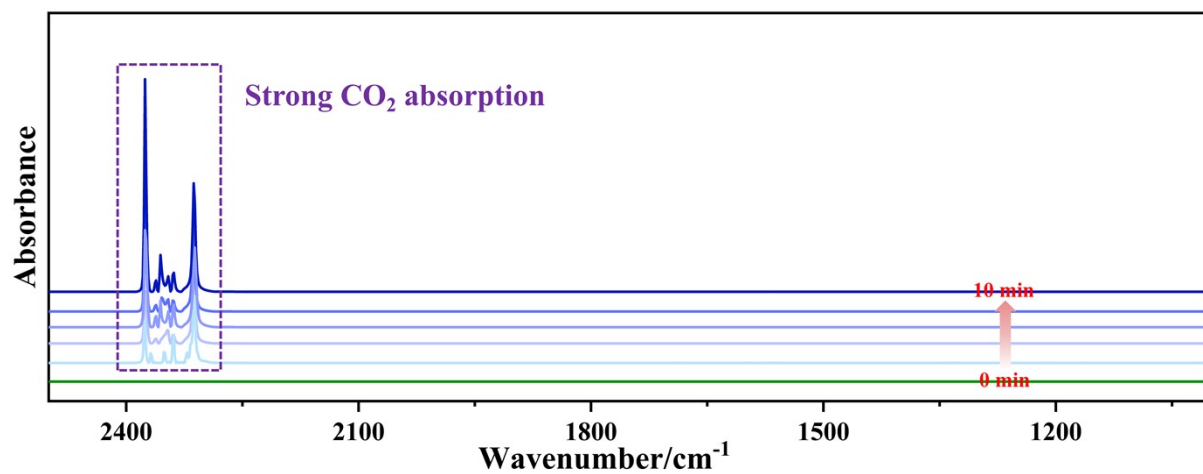

Figure S16. Infrared spectra of **2** before and after PCR reactions.

Figure S17. In-situ DRIFT spectra of catalyst **2** in CO_2 and H_2O atmosphere under dark conditions. The spectra were collected every 2 min.

References

1. Spackman, P. R.; Turner, M. J.; McKinnon, J. J.; Wolff, S. K.; Grimwood, D. J.; Jayatilaka, D.; Spackman, M. A., CrystalExplorer: a program for Hirshfeld surface analysis, visualization and quantitative analysis of molecular crystals. *J. Appl. Crystallogr.* **2021**, *54* (3), 1006-1011. https://doi.org/10.1107/S1600576721002910.

2. Sheldrick, G., Crystal structure refinement with SHELXL. *Acta Crystallographica Section C* **2015**, *71* (1), 3-8. https://doi/10.1107/S1399004714010372.

3. Klapötke, T. M.; Krumm, B.; Polbom, K.; Rienäcker, C. M., Synthesis and Characterization of Bromo- and Bromochloroplumbates(II). Crystal Structures of [Ph$_4$E]$_2$[Pb$_3$Br$_8$] (E = P, As) and [Ph$_4$P][PbBrCl$_2$] • CH$_3$CN. *Z. Naturforsch B* **2000**, *55* (5), 377-382. https://doi.org/10.1515/znb-2000-0506.

4. Brown, I. D., On measuring the size of distortions in coordination polyhedra. *Acta Crystallogr., Sect. B: Struct. Sci.* **2006**, *62* (4), 692-694. https://doi.org/10.1107/S010876810601322X.

5. Zhang, Y.; Wang, Y.; Zhao, L.; Yang, X.; Hou, C.-H.; Wu, J.; Su, R.; Jia, S.; Shyue, J.-J.; Luo, D.; Chen, P.; Yu, M.; Li, Q.; Li, L.; Gong, Q.; Zhu, R., Depth-dependent defect manipulation in perovskites for high-performance solar cells. *Energy Environ. Sci.* **2021**, *14* (12), 6526-6535. https://doi.org/10.1039/D1EE02287C.

6. Zynger, D. L.; Everton, M. J.; Dimov, N. D.; Chou, P. M.; Yang, X. J., Expression of Glypican 3 in Ovarian and Extragonadal Germ Cell Tumors. *Am. J. Clin. Pathol.* **2008**, *130* (2), 224-230. https://doi.org/10.1309/8DN7DQRDFB4QNH3N.

7. Bhosale, S. S.; Kharade, A. K.; Jokar, E.; Fathi, A.; Chang, S.-m.; Diau, E. W.-G., Mechanism of Photocatalytic CO$_2$ Reduction by Bismuth-Based Perovskite Nanocrystals at the Gas–Solid Interface. *J. Am. Chem. Soc.* **2019**, *141* (51), 20434-20442. https://doi.org/10.1021/jacs.9b11089.

8. Dong, J. P.; Xu, Y.; Zhang, X. G.; Zhang, H.; Yao, L.; Wang, R.; Zang, S. Q., Copper‐Sulfur‐Nitrogen Cluster Providing a Local Proton for Efficient Carbon Dioxide Photoreduction. *Angew. Chem. Int. Ed.* **2023**, e202313648. https://doi.org/10.1002/anie.202313648.

9. Chen, R.; Gao, G.; Luo, J., A water-stable organolead iodide material for overall photocatalytic CO$_2$ reduction. *Nano Research* **2022**, *15* (12), 10084-10089. https://doi.org/10.1007/s12274-022-4216-7.

10. Que, M.; Zhao, Y.; Pan, L.; Yang, Y.; He, Z.; Yuan, H.; Chen, J.; Zhu, G., Colloidal formamidinium lead bromide quantum dots for photocatalytic CO$_2$ reduction. *Mater. Lett.* **2021**, *282*, 128695. https://doi.org/10.1016/j.matlet.2020.128695.

11. Guo, N.-N.; Liu, Z.-L.; Mu, Y.-F.; Zhang, M.-R.; Yao, Y.; Zhang, M.; Lu, T.-B., In-situ growth of PbI$_2$ on ligand-free FAPbBr$_3$ nanocrystals to significantly ameliorate the stability of CO$_2$ photoreduction. *Chin. Chem. Lett.* **2022**, *33* (6), 3039-3042. https://doi.org/10.1016/j.cclet.2021.09.033.

12. Que, M.; Zhao, Y.; Yang, Y.; Pan, L.; Lei, W.; Cai, W.; Yuan, H.; Chen, J.; Zhu, G., Anchoring of Formamidinium Lead Bromide Quantum Dots on Ti$_3$C$_2$ Nanosheets for Efficient Photocatalytic Reduction of CO$_2$. *ACS Appl. Mater. Inter.* **2021**, *13* (5), 6180-6187. https://doi.org/10.1021/acsami.0c18391.

13. Mu, Y.-F.; Zhang, C.; Zhang, M.-R.; Zhang, W.; Zhang, M.; Lu, T.-B., Direct Z-Scheme Heterojunction of Ligand-Free FAPbBr$_3$/α-Fe$_2$O$_3$ for Boosting Photocatalysis of CO$_2$ Reduction Coupled with Water Oxidation. *ACS Appl. Mater. Inter.* **2021,** *13* (19), 22314-22322. https://doi.org/10.1021/acsami.1c01718.

14. Lee, H.; Kim, M.; Lee, H., Reducing the Photodegradation of Perovskite Quantum Dots to Enhance Photocatalysis in CO$_2$ Reduction. *Catalysts* **2021,** *11* (1), 61. https://doi.org/10.3390/catal11010061.

15. Wu, L. Y.; Mu, Y. F.; Guo, X. X.; Zhang, W.; Zhang, Z. M.; Zhang, M.; Lu, T. B.,

Encapsulating Perovskite Quantum Dots in Iron‑Based Metal‑Organic Frameworks

(MOFs) for Efficient Photocatalytic CO$_2$ Reduction. *Angew. Chem. Int. Ed.* **2019,** *58* (28), 9491-9495. https://doi.org/10.1002/anie.201904537.

16. Xu, S.; Yang, L.; Wei, Y.; Jia, Y.; Hu, M.; Bai, L.; Zhang, J.; Li, X.; Wei, S.; Lu, J., Monochromatic light-enhanced photocatalytic CO$_2$ reduction based on exciton properties of two-dimensional lead halide perovskites. *Dalton Trans.* **2022,** *51* (20), 8036-8045. https://doi.org/10.1039/D2DT00972B.

17. Sheng, J.; He, Y.; Li, J.; Yuan, C.; Huang, H.; Wang, S.; Sun, Y.; Wang, Z.; Dong, F., Identification of Halogen-Associated Active Sites on Bismuth-Based Perovskite Quantum Dots for Efficient and Selective CO$_2$-to-CO Photoreduction. *ACS Nano* **2020,** *14* (10), 13103-13114. https://doi.org/10.1021/acsnano.0c04659.

18. Wu, D.; Zhao, X.; Huang, Y.; Lai, J.; Yang, J.; Tian, C.; He, P.; Huang, Q.; Tang, X., Synthesis and CO$_2$ Photoreduction of Lead-Free Cesium Bismuth Halide Perovskite Nanocrystals. *J. Phys. Chem. C* **2021,** *125* (33), 18328-18333. https://doi.org/10.1021/acs.jpcc.1c05110

19. Liu, Z.-L.; Liu, R.-R.; Mu, Y.-F.; Feng, Y.-X.; Dong, G.-X.; Zhang, M.; Lu, T.-B., In

Situ Construction of Lead‑Free Perovskite Direct Z-Scheme Heterojunction

Cs$_3$Bi$_2$I$_9$/Bi$_2$WO$_6$ for Efficient Photocatalysis of CO$_2$ Reduction. *Solar RRL* **2021,** *5*, 2000691. https://doi.org/10.1002/solr.202000691.

20. Cui, Z.; Wang, P.; Wu, Y.; Liu, X.; Chen, G.; Gao, P.; Zhang, Q.; Wang, Z.; Zheng, Z.; Cheng, H.; Liu, Y.; Dai, Y.; Huang, B., Space-confined growth of lead-free halide perovskite Cs$_3$Bi$_2$Br$_9$ in MCM-41 molecular sieve as an efficient photocatalyst for CO$_2$ reduction at the gas−solid condition under visible light. *Appl. Catal. B: Environ.* **2022,** *310*, 121375. https://doi.org/10.1016/j.apcatb.2022.121375.

21. Zhang, Z.; Wang, M.; Chi, Z.; Li, W.; Yu, H.; Yang, N.; Yu, H., Internal electric field engineering step-scheme–based heterojunction using lead-free Cs$_3$Bi$_2$Br$_9$ perovskite–modified In$_4$SnS$_8$ for selective photocatalytic CO$_2$ reduction to CO. *Appl. Catal. B Environ.* **2022,** *313*, 121426. https://doi.org/10.1016/j.apcatb.2022.121426.

22. Fu, H.; Liu, X.; Wu, Y.; Zhang, Q.; Wang, Z.; Zheng, Z.; Cheng, H.; Liu, Y.; Dai, Y.; Huang, B.; Wang, P., Construction of a bismuth-based perovskite direct Z-scheme heterojunction Au-Cs$_3$Bi$_2$Br$_9$/V$_2$O$_5$ for efficient photocatalytic CO$_2$ reduction. *Appl. Surf. Sci.* **2023,** *622*, 156964. https://doi.org/10.1016/j.apsusc.2023.156964.

23. Zhang, Z.; Li, D.; Chu, Y.; Xu, J., Mesoporous α-Fe$_2$O$_3$ nanostructures decorated with perovskite Cs$_3$Bi$_2$Br$_9$ quantum dots as an S-scheme photocatalyst for efficient charge transfer

and CO_2 conversion. *Appl. Surf. Sci.* **2023,** *640*, 158468. https://doi.org/10.1016/j.apsusc.2023.158468.

24. Zhou, L.; Xu, Y. F.; Chen, B. X.; Kuang, D. B.; Su, C. Y., Synthesis and Photocatalytic Application of Stable Lead-Free $Cs_2AgBiBr_6$ Perovskite Nanocrystals. *Small* **2018,** *14* (11), e1703762. https://doi.org/10.1002/smll.201703762.

25. Zhang, Z.; Wang, B.; Zhao, H.-B.; Liao, J.-F.; Zhou, Z.-C.; Liu, T.; He, B.; Wei, Q.; Chen, S.; Chen, H.-Y.; Kuang, D.-B.; Li, Y.; Xing, G., Self-assembled lead-free double perovskite-MXene heterostructure with efficient charge separation for photocatalytic CO_2 reduction. *Appl. Catal. B: Environ.* **2022,** *312*, 121358. https://doi.org/10.1016/j.apcatb.2022.121358.

26. Ding, L.; Bai, F.; Borjigin, B.; Li, Y.; Li, H.; Wang, X., Embedding $Cs_2AgBiBr_6$ QDs into Ce-UiO-66-H to in situ construct a novel bifunctional material for capturing and photocatalytic reduction of CO_2. *Chem. Eng. J.* **2022,** *446*, 137102. https://doi.org/10.1016/j.cej.2022.137102.

27. Wang, J.; Cheng, H.; Wei, D.; Li, Z., Ultrasonic-assisted fabrication of $Cs_2AgBiBr_6/Bi_2WO_6$ S-scheme heterojunction for photocatalytic CO_2 reduction under visible light. *Chinese J. Catal.* **2022,** *43* (10), 2606-2614. https://doi.org/10.1016/S1872-2067(22)64091-9.

28. Mahmoud Idris, A.; Zheng, S.; Wu, L.; Zhou, S.; Lin, H.; Chen, Z.; Xu, L.; Wang, J.; Li, Z., A heterostructure of halide and oxide double perovskites $Cs_2AgBiBr_6/Sr_2FeNbO_6$ for boosting the charge separation toward high efficient photocatalytic CO_2 reduction under visible-light irradiation. *Chem. Eng. J.* **2022,** *446*, 137197. https://doi.org/10.1016/j.cej.2022.137197.

29. Purohit, S.; Shyamal, S.; Saini, S. K.; Yadav, K. L.; Kumar, M.; Satapathi, S., Photocatalytic CO_2 Reduction Using an Amorphous TiO_2-Encapsulated $Cs_2AgBiBr_6$ Nanocrystal: Selective Methane Formation. *Energy Fuels* **2022,** *36* (19), 12170-12180. https://doi.org/10.1021/acs.energyfuels.2c02484.

30. Kumar, S.; Hassan, I.; Regue, M.; Gonzalez-Carrero, S.; Rattner, E.; Isaacs, M. A.; Eslava, S., Mechanochemically synthesized Pb-free halide perovskite-based $Cs_2AgBiBr_6$–Cu–RGO nanocomposite for photocatalytic CO_2 reduction. *J. Mater. Chem. A* **2021,** *9* (20), 12179-12187. https://doi.org/10.1039/D1TA01281A.